



**Observation of direct magneto-dielectric behaviour in
Lu₃Fe₅O_{12-δ} above room-temperature**

Journal:	<i>Physical Chemistry Chemical Physics</i>
Manuscript ID:	CP-ART-05-2015-002719
Article Type:	Paper
Date Submitted by the Author:	11-May-2015
Complete List of Authors:	Periyasamy, Manimuthu; University of Madras, Department of Nuclear Physics Ravidran, Vidya; Institute of Mathematical Sciences, ; University of Oslo, Center for Materials Sciences and Nanotechnology, Department of Chemistry Ravindran, Ponniah; University of Oslo, Department of Chemistry; Central University of Tamil Nadu, Fjellvåg, Helmer; University of Oslo, Chemistry Chakrawarthy, Venkateswaran; University of Madras,

SCHOLARONE™
Manuscripts

Observation of direct magneto-dielectric behaviour in $\text{Lu}_3\text{Fe}_5\text{O}_{12-\delta}$ above room-temperature

P. Manimuthu,¹ R. Vidya,^{2,3,4} P. Ravindran,^{3,5} H. Fjellvåg,³ and
C. Venkateswaran^{1*}

¹Department of Nuclear Physics, University of Madras, Guindy Campus, Chennai- 600 025,
India

²Institute of Mathematical Sciences, Taramani, Chennai- 600 113, India

³Centre for Materials Science and Nanotechnology, Department of Chemistry,
University of Oslo, Box 1033 Blindern, N-0315 Oslo, Norway

⁴Department of Medical Physics, Anna University, Chennai- 600 025, India

⁵Department of Physics, Central University of Tamil Nadu, Thiruvavur- 610 004, India

*E-mail: cvunom@hotmail.com

Tel.: +91- 044-2220 2803; Fax: +91- 044-2235 3309

ABSTRACT

The coupling of dielectric and magnetic order is highly nontrivial and seldom observed in rare-earth iron garnets. Careful investigations on polycrystalline $\text{Lu}_3\text{Fe}_5\text{O}_{12-\delta}$, prepared by the solid state route, establish a direct correlation between the magnetic and dielectric order parameters. A dielectric anomaly at the magnetic ordering temperature supports this correlation. The dielectric permittivity at various magnetic fields is measured using an indigenously developed connector setup. $\text{Lu}_3\text{Fe}_5\text{O}_{12-\delta}$ exhibits a magneto-dielectric coupling of $\sim 6\%$ at room temperature, which is significant in case of a single-phase magneto-dielectric material at low fields. Rietveld refinement of the X-ray diffraction pattern, Bond valence sum method, Mössbauer spectroscopy, and X-ray

photoelectron spectroscopy indicate two different oxidation states of Fe. Complete structural optimizations performed using density functional theory establishes ferrimagnetic ground state and provides structural parameters in agreement with experimental values. Electronic structure analysis shows that $\text{Lu}_3\text{Fe}_5\text{O}_{12}$ exhibits insulating behavior both in ferromagnetic and ferrimagnetic configurations. The capability of $\text{Lu}_3\text{Fe}_5\text{O}_{12-\delta}$ to exhibit room temperature magneto-dielectric response is a key factor in designing and fabricating various electronic devices and sensors.

Keywords: Rare-earth iron garnets, Oxygen vacancy, Multiferroic, Mössbauer spectroscopy, X-ray photoelectron spectroscopy, Density functional theory

1. Introduction

Multiferroic materials have been attracting much interest recently because of the coexistence of ferroelectric, ferromagnetic and ferroelastic orders.¹⁻⁷ The coupling between ferroelectric and ferromagnetic orders have attracted renewed interest due to the spectacular discoveries of giant magneto-electric (ME) [inducement of electric polarization by magnetic field (H) or vice versa] and magneto-dielectric (MD) effects [H-induced change in dielectric permittivity] in these materials.⁸⁻¹⁰ The MD effect has recently been introduced to classify certain magnetic materials that possess neither spontaneous polarization nor satisfy the symmetry constraints, for linear magneto-electric effect, but still show some kind of coupling between the dielectric properties and magnetization.¹¹ The MD phenomenon itself is attractive for practical applications without ME coupling. A number of device applications have been suggested based on the MD effect, including multiple state memory elements, electric field controlled ferromagnetic resonance device, and variable transducers with either magnetically modulated piezoelectricity or electrically modulated piezomagnetism.¹² Studies

on MD effect were mainly carried out on single phase materials, which show dielectric change under an external magnetic field.^{1-3,7,13} The possibility of tuning the dielectric permittivity by an external magnetic field opens up new prospects for the basic understanding of multiferroic materials and for the design of devices based on them. But the magnetic field required for producing this effect is quite high, of the order of several tesla.^{1-3,7,13,14} However, for the utilization of this effect in the above-mentioned devices, materials exhibiting MD effect at low magnetic field (< 1 T) are essential. The realization of the MD effect with a small external magnetic field is highly nontrivial and such MD materials are still rare.¹⁵⁻¹⁸ Rare-earth Iron Garnets (RIG) with their amazingly interesting properties attract significant attention at this juncture. The materials belonging to this class were found to exhibit relatively good magneto-dielectric effect even for a low applied magnetic field. At low magnetic fields, induced MD effect have been reported with values reaching 13 % at 0.5 T and 10 K in $\text{Y}_3\text{Fe}_5\text{O}_{12}$ ¹⁹ and 3 % for $H < 0.2$ T below 30 K in $\text{Tb}_3\text{Fe}_5\text{O}_{12}$ ¹⁷. However, most of the practical applications demand MD effect at room temperature.

$\text{Lu}_3\text{Fe}_5\text{O}_{12}$ is one such compound which exhibits low field MD response at room temperature.²⁰ $\text{Lu}_3\text{Fe}_5\text{O}_{12}$, which belongs to the RIG family, has cubic symmetry with the space group, $Ia-3d$. The unit cell of $\text{Lu}_3\text{Fe}_5\text{O}_{12}$ is composed of lutetium-oxygen and iron-oxygen clusters forming three dodecahedral (LuO_8), three tetrahedral (FeO_4) and two octahedral (FeO_6) sites. The Fe^{3+} ions occupy the $16a$ Wyckoff position in the octahedral (0 0 0) site and $24d$ Wyckoff position in the tetrahedral (0.375 0 0.25) site. The Fe^{3+} ions in the octahedral and tetrahedral sites are denoted as $\text{Fe}1^o$ and $\text{Fe}2^t$, respectively. The Lu ions are distributed over the $24c$ (0.125 0 0.25) Wyckoff position in the dodecahedral site and O is in the (-0.0255 0.0592 0.1514) $96h$ site. Fe ions in the tetrahedral and octahedral sites contribute to the magnetic properties which are coupled antiparallel with each other (Fig. 1). The Lu in the dodecahedral site does not possess magnetic moment due to the absence of

unpaired electrons as Lu has $4f^{14}$ configuration. In general, the material is recognized and evidenced as a single phase MD material and therefore should have a dielectric anomaly at the magnetic ordering temperature (irrespective of the type of magnetic ordering).^{16,21-23} As of now, there is no experimental evidence showing the direct coupling between magnetic and dielectric properties of $\text{Lu}_3\text{Fe}_5\text{O}_{12}$. But such a behaviour is possible in $\text{Lu}_3\text{Fe}_5\text{O}_{12}$ which has a significant range of non-stoichiometry compared to other RIGs.^{20,24,25} The non-stoichiometry is accommodated in $\text{Lu}_3\text{Fe}_5\text{O}_{12}$ by the formation of oxygen vacancies. The formal oxidation state of Fe ions in $\text{Lu}_3\text{Fe}_5\text{O}_{12}$ is 3+ but during the high temperature process the oxidation state changes to 2+ owing to the loss in oxygen content.^{19,20,26,27} It is well known that the varying oxidation state of transition metal ions greatly affects the physical properties.^{19,20,26-29} Hence, this material is of particular interest, as both the dielectric and magnetic order parameters have a common origin i.e., Fe ions facilitating good coupling in $\text{Lu}_3\text{Fe}_5\text{O}_{12}$. This paper reports the magnetic, dielectric, and MD properties of polycrystalline $\text{Lu}_3\text{Fe}_5\text{O}_{12}$ and explores the possible presence of Fe in mixed valence states, based on the observed results.

2. Materials and Method of Synthesis

$\text{Lu}_3\text{Fe}_5\text{O}_{12}$ ceramics were prepared employing a standard, solid-state reaction method. Raw Lu_2O_3 (99.9 %) and Fe_2O_3 (99.95 %) powders, weighed in stoichiometric proportions, were directly mixed together using an agate mortar and pestle for 5 hours. The resulting powder was calcined at 1173 K for 2 hours in air. The standard free energy formation temperature for $\text{Lu}_3\text{Fe}_5\text{O}_{12}$ compound is reported to be 1473 K.²⁴ Hence; $\text{Lu}_3\text{Fe}_5\text{O}_{12}$ ceramics were obtained by sintering at 1473 K for 5 hours in air. High temperature sintering is a diffusion controlled process by which bonding of particles in a mass of powder in the solid state occurs by atomic or molecular attraction through the application of heat. The densification is due to the decrease in the surface area and therefore a reduction in the free energy of the system during sintering is occurred. High temperature sintering creates low

oxygen pressure inside the furnace under normal atmospheric conditions. Lu-Fe-O system belongs to the D-type of lanthanoid-Fe-O compound. The phase diagram of Lu-Fe-O shows four stable phases: LuFe_2O_4 (spinel), LuFeO_3 (perovskite), $\text{Lu}_2\text{Fe}_3\text{O}_7$ and $\text{Lu}_3\text{Fe}_5\text{O}_{12}$ (garnet) at elevated temperatures under controlled oxygen partial pressures.³⁰ Lu-Fe-O compounds are very sensitive to the atmosphere as reported elsewhere.^{20,24} Due to the low oxygen pressure generated by high-temperature sintering, oxygen vacancies are formed in $\text{Lu}_3\text{Fe}_5\text{O}_{12}$ lattice.

3. Experimental Techniques

The purity and crystallinity of the sintered sample were confirmed from the X-ray diffractometer measurements (Bruker D2 PHASER) using Cu- $K\alpha$ radiation and the pattern was refined according to the Rietveld method using the General Structure Analysis System (GSAS) program.^{31,32} Bond valence sum method has been used to determine the oxidation state of Fe ions, based on crystallographically determined Fe-O bond distances. The oxidation state and site occupancy of Fe ions were identified through Mössbauer spectroscopy (Nucleonix, India). Field dependent (Lakeshore VSM 7410) and temperature dependent (EG & G PARC 4500) magnetic properties were determined using a vibrating sample magnetometer (VSM). The combination states of Fe 2*p* electrons were analyzed through X-ray photoelectron spectroscopy (XPS) (Omicron Nanotechnology, Germany). The dielectric properties were measured as a function of temperature (353 K to 723 K) using an impedance analyzer (Solatron SI 1260 impedance/gain phase analyzer) in the frequency range of 1 kHz to 1 MHz. The magneto-dielectric measurements were done with the help of an indigenously designed connector setup.³³ The salient feature of this setup is that, it is incorporated with the already existing instruments like VSM and impedance analyzer used in this study.

3.1. Computational Methodology

First principles DFT calculations were performed using the Vienna Ab-initio simulation package (VASP)³⁴ within the projector augmented wave (PAW) method³⁵ as implemented by

Kresse and Joubert.³⁶ The Kohn-Sham equations³⁷ were solved self-consistently using an iterative matrix diagonalization method. This is based on a band-by-band preconditioned conjugate gradient method³⁸ with an improved Pulay mixing³⁹ to efficiently obtain the ground-state electronic structure. The forces on the atoms were calculated using the Hellmann-Feynman theorem and they are used to perform a conjugate gradient relaxation. Structural optimizations were continued until the forces on the atoms had converged to less than 1 meV/Å and the pressure on the cell had minimized within the constraint of constant volume and the total energy convergence. We have used an energy tolerance of 10^{-6} eV for SCF calculations. The calculations were performed within periodic boundary conditions allowing the expansion of the crystal wave functions in terms of a plane-wave basis set. The Generalized Gradient Approximation (GGA)⁴⁰ includes the effects of local gradients in the charge density for each point which generally gives better equilibrium structural parameters. In order to include strong correlation effects GGA+ U calculations have been done as implemented in VASP-PAW method using the Dudarev scheme.⁴¹

In this basis, we treated explicitly 3 valence electrons for Lu ($5d^16s^2$), 8 for Fe ($3d^64s^2$), and 6 for oxygen ($2s^22p^4$). Brillouin zone integrations are performed with a Gaussian broadening⁴² of 0.1 eV during all structural optimizations. We have performed a series of test calculations by gradually increasing energy cut-off from 275 eV. Though we found that the total-energy converges to an energy cut-off value of 450 eV, we used 550 eV cut-off in an effort to obtain more accurate results with an optimum usage of computational resources. These calculations are performed with a $4\times 4\times 4$ Monkhorst-Pack k-point mesh. The structures were fully relaxed for all volumes considered in the present calculations using force as well as stress minimization. Experimentally established structural data were used as input for the calculations. We have carried out calculations on non-magnetic, ferromagnetic and anti-ferromagnetic configurations.

4. Results and Discussion

4.1. Structural Characterization

Structural characterization of the prepared sample was carried out using X-ray diffractometer. Sharp reflection peaks are observed, indicating that the sample is properly sintered to good crystallinity. The pattern has then been refined according to the Rietveld method using the GSAS program (Fig. 2). The refinement parameters such as atomic coordination factor, multiplicity factor, occupancy, B-factor, and cell parameters are listed in Table I. The reliability factors ($\chi^2 = 1.98$, $R_p = 2.1$, $R_{wp} = 2.8$, $R_{exp} = 3.4$) obtained from Rietveld refinement of XRD pattern indicate a better fit between the experimental and calculated patterns of cubic ($Ia-3d$) system. From the refinement, three different crystallographic Fe-O bond distances are obtained, i.e., 1.828 Å corresponds to tetrahedral site, 2.038 Å and 2.045 Å correspond to octahedral site. In general, only two Fe-O bond lengths are obtained which means, Fe ion coordinated with four oxygen atoms in the tetrahedral site with a bond distance of 1.88 Å and in octahedral site by six oxygen atoms with a bond distance of 2.02 Å.⁴³⁻⁴⁶ Therefore, the existence of another bond length in the octahedral site may be due to two different oxidation states of Fe ion. Using the value of ionic radii of 1.38 Å and 1.4 Å of oxygen in tetrahedral and octahedral sites, we obtain the ionic radii value of 0.45 Å, 0.638 Å and 0.645 Å for Fe ion with respect to the calculated Fe-O bond distances. According to Shannon's theory,⁴⁷ the ionic radius value of 0.45 Å corresponds to Fe³⁺ in tetrahedral site. The other two ionic radii 0.638 Å and 0.645 Å correspond to two different oxidation states of Fe ion in the octahedral site, which is due to the formation of oxygen vacancies as reported elsewhere.^{24,47} In a widely accepted view of the microscopic description of oxygen vacancy formation, some of the Fe³⁺ ions are reduced to Fe²⁺ in the octahedral site for charge neutrality in the crystal structure.⁴⁸⁻⁵¹ Since, the ionic radii of Fe²⁺ is slightly greater than that of Fe³⁺ ion, two different Fe-O bond distances are

found to vary accordingly, corresponding to octahedral site. Hence in this crystal system, tetrahedral sublattice is completely occupied by Fe^{3+} ions while the octahedral sublattice is shared by the Fe^{3+} and Fe^{2+} ions. Though the material has a significant range of non-stoichiometry due to oxygen vacancy, no major variation in cell parameters ($a = b = c = 12.279(2) \text{ \AA}$ and Volume = $1851.1(1) \text{ \AA}^3$) are observed, indicating that the oxygen vacancies could be isolated defect centers instead of vacancy clusters.

4.2. Bond valence sum method

Bond length values calculated from crystallographic distances are used to predict the correct oxidation state of the Fe ion using bond valence sum method.⁵²⁻⁵⁸ Bond valences (s) are calculated according to the following equation,

$$S = \exp^{[(r_0 - r)/B_0]} \quad (1)$$

where r is the observed bond distance and r_0 and B_0 are empirically determined parameters.⁵² From the Rietveld refinement of XRD pattern, the obtained bond distance values are 2.038 \AA and 2.045 \AA for octahedral site ($\text{Fe}^{1^{\circ}}\text{-O1}$) and 1.828 \AA for tetrahedral site ($\text{Fe}^{2^{\dagger}}\text{-O1}$). The two bond distances corresponding to octahedral site are due to two different oxidation states of Fe ion as discussed previously and therefore are classified for convenience as $\text{Fe}_1^{1^{\circ}}\text{-O1} = 2.038 \text{ \AA}$ and $\text{Fe}_2^{1^{\circ}}\text{-O2} = 2.045 \text{ \AA}$. Bond valences for each Fe-O bond are calculated from the above equation (1) using the value of $r_0 = 1.759 \text{ \AA}$ for $\text{Fe}^{3+}\text{-O}$, $r_0 = 1.734 \text{ \AA}$ for $\text{Fe}^{2+}\text{-O}$ and $B_0 = 0.37 \text{ \AA}$.⁵⁹⁻⁶¹ The calculated bond valences are 2.83, 2.58, and 3.25 corresponding to $\text{Fe}_1^{1^{\circ}}$, $\text{Fe}_2^{1^{\circ}}$, and $\text{Fe}^{2^{\dagger}}$, which could be approximated to the known oxidation states of 3+, 2.5+, and 3.5+, respectively.

4.3. Magnetic studies

4.3.1. Mössbauer Measurements

Fig. 3 shows the Mössbauer spectrum of $\text{Lu}_3\text{Fe}_5\text{O}_{12-\delta}$ at room temperature arising due to Fe in octahedral and tetrahedral sites. The dots represent the experimental data and the

continuous curves represent the fitting of the experimental data. The Fe ions are magnetically ordered and are present in three different environments as evidenced from the observation of three sextets in the spectrum corresponding to tetrahedral and octahedral sites. The hyperfine magnetic fields (HF) give a clear insight into the site occupancy by providing information on which site a particular Fe ion occupies. The hyperfine magnetic fields were found to be in the order of HF (octahedral) > HF (tetrahedral).^{62,63} The obtained hyperfine magnetic field values of 48 T and 51 T correspond to the octahedral site and 38 T corresponds to the tetrahedral site.⁶⁴ Based on the previous reports, the sextet of smallest isomer shift (IS) of 0.19 mm/s with a HF of 38 T is a characteristic feature of Fe³⁺ ions in the tetrahedral site (Fe^{2t}). The other two sextets with relatively larger isomer shifts i.e., 0.42 mm/s and 0.45 mm/s with the HF of 51 T and 48 T correspond to Fe₁1^o and Fe₂1^o, respectively.^{65,66}

4.3.2. Vibrating Sample Magnetometer (VSM) Measurements

(a) Field dependent magnetization (M-H) curve

Fig. 4(a) shows *M-H* curves of Lu₃Fe₅O_{12-δ} ceramics at 30 K and 300 K, exhibiting clear ferrimagnetic behaviour. Magnetization starts saturating at a relatively low field of ~0.2 T with a saturation magnetization (*M_S*) of 23 emu/g (32.8 μ_B/unit cell) and 18 emu/g (25.6 μ_B/unit cell) at 30 K and 300 K, respectively. Also, it is found that the temperature effect on *M_S* is smaller than those of other garnets due to the diamagnetism of Lu³⁺. The loop at 30 K shows a larger hysteresis compared to the loop at 300 K, which is due to the changes in the magnetic domain wall motion (or) domain rotation.¹⁷

(b) Temperature dependent magnetization (M-T) plot

The Curie temperature, *T_C*, was determined from the temperature dependent magnetization decay of the sample as depicted in Fig. 4(b). This was done by heating the sample from 303 K to 573 K in regular steps with a constant applied field of 100 Oe. From Fig. 4(b), it is seen that, the orientation of the magnetic moments decrease with increasing

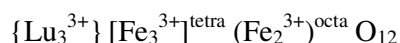
temperature and finally vanishes around 550 K which is a characteristic feature of the material undergoing a Curie transition or phase transition. Curie transition i.e., a transition from paramagnetic to ferrimagnetic state occurs when the magnetic moment changes from zero to a non-zero value. The Kink-Point method (plotting $-\frac{dM}{dT}$ as a function of temperature) also shows that T_C to be around 550 K (inset of Fig. 4(b)). Below T_C , the magnetic moment of Fe ions in both the tetrahedral and octahedral sites are aligned anti-parallel to each other with different magnitudes causing a resultant magnetic moment making the material to be ferrimagnetic. Above T_C , the long range magnetic ordering in the material disappears.

4.3.3. Discussion on the Mössbauer and VSM results

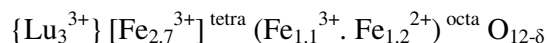
From the Mössbauer spectrum, it becomes difficult to accurately determine the oxidation state of Fe ions in the octahedral site whether it is Fe^{3+} or Fe^{2+} , based on the obtained isomer shift values (i.e., 0.42 mm/s and 0.45 mm/s). The isomer shift value is easily influenced by parameters like temperature, pressure and other factors like the coordination number, bond length, spin state, and nature of bonding interaction with neighbors, etc.⁶⁷ If the Fe ions were to exist only in the oxidation state of 3+, the resulting magnetic moment as per the calculations (from the relative area fraction of Fe ions in the Mössbauer spectrum) should have the value of $16 \mu_B/\text{unit cell}$. But $M-H$ results clearly show the magnitude of magnetic moment to be $25.6 \mu_B/\text{unit cell}$. This proves the existence of two different isomer shift values corresponding to two different oxidation states of Fe ions in the octahedral site. From the Mössbauer spectrum of the two sextets, the one with the isomer shift of 0.42 mm/s with the HF of 51 T corresponds to Fe^{3+} ions ($\text{Fe}_1^{1^0}$) while the other one with the isomer shift of 0.45 mm/s with the HF of 48 T corresponds to Fe^{2+} ion ($\text{Fe}_2^{1^0}$). The loss of oxygen during sintering might have reduced some of the Fe^{3+} ions to Fe^{2+} ions giving rise to higher values for the isomer shift and smaller values for the hyperfine fields. Hence, the Fe^{2+} ions occupy the octahedral site (24 %) while the Fe^{3+} ions exist both in the tetrahedral (54 %) and

octahedral (22 %) sites. The relative area of Fe^{2+} and Fe^{3+} ions are 24 % and 76 %, respectively.

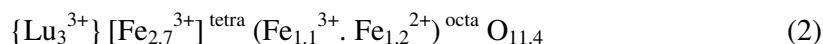
Considering the relative area fraction of each Fe ion in the Mössbauer spectrum, the contribution from the number of Fe ions to a unit cell is calculated. The contribution from Fe^{3+} is 21.6 (54 %) at the tetrahedral site and 8.8 (22 %) at the octahedral site, whereas the contribution from Fe^{2+} ions is 9.6 (24 %) at the octahedral site. The general expression for one formula unit is,



Based on the above results, the formula unit can be obtained as,



The magnetic moments of Fe ions within each site are coupled parallel to each other, whereas in tetrahedral and octahedral sites the moments are antiparallel to each other. This antiparallel coupling of two unequal sites gives ferrimagnetic ordering. The direction of total magnetic moment is the same as that of moment of Fe^{3+} ions at the tetrahedral site. The derived magnetic moment as per the calculation (using Mössbauer result) for a unit cell is $25.6 \mu_B/\text{unit cell}$, which is in good agreement with the observed M_S value of $M-H$ results ($25.6 \mu_B/\text{unit cell}$). Considering the number of Fe^{2+} ions resulting from the oxygen vacancies, the calculated oxygen vacancies per formula unit is $\delta = 0.6$ (single oxygen vacancy should create two Fe^{2+} ions) and hence the general expression of the compound in the defect state can be written as,



4.4. X-ray photoelectron spectroscopy (XPS) study

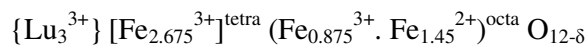
X-ray photoelectron spectroscopy, a highly used surface-sensitive technique^{68,69} has been employed to identify the overall oxidation or chemical state of Fe ions in the prepared $\text{Lu}_3\text{Fe}_5\text{O}_{12-\delta}$ sample. The high resolution XPS peaks of Fe $2p_{3/2}$ and Fe $2p_{1/2}$ are shown in

Fig. 5. The area of Fe $2p_{3/2}$ peak is greater than that of Fe $2p_{1/2}$ because of its spin-orbit (j-j) coupling; Fe $2p_{3/2}$ has degeneracy of four states whilst Fe $2p_{1/2}$ has only two.⁷⁰ In addition to that, the peaks have broad envelope with shoulder on the low binding energy side. The peaks have been fitted using Gaussian-Lorentzian curve fitting method. When fitted with a single peak, the overall fit does not match with the experimental data. The best fit was obtained when each broad peak has been deconvoluted into two distinct peaks and is clearly shown in Fig. 5. This confirms the existence of Fe ion in two different oxidation states. Charge correction was carried out using the C1s peak with a fixed value of 284.6 eV. The reported binding energies of Fe $2p_{3/2}$ and Fe $2p_{1/2}$ have been investigated by many researchers and the values are between 710.6 eV - 711.2 eV for Fe $2p_{3/2}$ and 724 eV - 724.6 eV for Fe $2p_{1/2}$.⁷¹⁻⁷³ The Fe spectrum has associated satellite peaks which are located approximately 8 eV higher than the main Fe $2p_{3/2}$ peak. The fitted peak positions correspond to the binding energy values of 709.1 eV and 710.8 eV for Fe $2p_{3/2}$ peak, and 722.7 eV and 724.4 eV for Fe $2p_{1/2}$ peak. It is well known that 709.1 eV and 722.7 eV are characteristics of Fe²⁺, and 710.8 eV and 724.4 eV of Fe³⁺. By evaluating the peak area, the estimated ratio of Fe²⁺ and Fe³⁺ is found to be 29 % and 71 %, respectively.

4.4.1. Combined XPS and VSM results

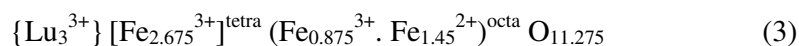
The XPS Fe $2p_{3/2}$ spectrum of the two peaks, the one with the binding energy of 710.8 eV corresponds to Fe³⁺ ion while the other with the binding energy value of 709.1 eV corresponds to Fe²⁺ ion. The loss of oxygen during sintering might have reduced some of the Fe³⁺ ions to Fe²⁺ ions. Considering the relative area fraction of each Fe ion in the XPS spectrum, the contribution from the number of Fe ions to a unit cell is calculated. The contribution from Fe³⁺ is 21.4 (53.5 %) at the tetrahedral site and 7 (17.5 %) at the octahedral site, whereas the contribution from Fe²⁺ ions is 11.6 (29 %) at the octahedral site.

Based on the above results, the formula unit can be obtained as,



The derived magnetic moment as per the calculation (using XPS result) for a unit cell is 25.6 μ_B /unit cell, which is in good agreement with the observed M_S value of $M-H$ result 18 emu/g (25.6 μ_B /unit cell). Considering the number of Fe^{2+} ions resulting from the defect, the calculated oxygen vacancies is 5.8 per unit cell (single oxygen vacancy should create two Fe^{2+} ions).

The general expression of the compound in the defect state can be written as,



4.5. Iodometric titration

The overall oxygen stoichiometry was estimated to be 11.5 ± 0.02 from the iodometric titration by the standardization of sodium thiosulfate using potassium dichromate with starch as the indicator.⁷⁴ Though there is a discrepancy in the determined oxygen content from Mössbauer (*eqn. 2*), XPS (*eqn. 3*) and iodometric titration results, the presence of off-stoichiometry is clearly evidenced from these results.

4.6. Density functional theory (DFT) calculations

We have performed complete structural optimization (including stress and force minimizations) on $\text{Lu}_3\text{Fe}_5\text{O}_{12}$ for non-magnetic, ferromagnetic, and anti-ferromagnetic configurations, by including GGA+ U functionals. It may be noted that for simple GGA calculation, the system did not converge in a magnetic configuration. However inclusion of GGA+ U functional (with a U value of 6.0 eV and $J = 1.0$ eV) lead to significant exchange splitting, indicating that $\text{Lu}_3\text{Fe}_5\text{O}_{12}$ is a strongly-correlated oxide. The antiferromagnetic configuration is lower in energy by 3.7 eV and 5.1 eV than ferromagnetic and non-magnetic configurations, respectively. However, as determined by experimental observations, $\text{Fe}^{1\circ}$ magnetic moments are not completely cancelled by $\text{Fe}^{2\text{t}}$ moments, resulting in ferrimagnetic state. The optimized lattice constant and atom positions are given in Table II. It can be seen

that theoretically calculated lattice constant (12.390 Å) is over-estimated by 2.75 % than experimentally determined lattice constant. DFT calculations using GGA functionals normally tend to overestimate volume by ~3 %. The calculated Fe1^o-O1 and Fe2^t-O1 bond lengths are 2.03 and 1.88 Å, respectively, in good agreement with the experimental values.

The magnetic moments calculated at ferromagnetic and ferrimagnetic configurations for various U values are given in Table III. In ferromagnetic configuration, Fe1^o and Fe2^t sites have magnetic moments of 4.43 μ_B and 4.29 μ_B , respectively and total magnetic moment is 24.49 μ_B /f.u for $U=6$ eV & $J=1$ eV. Owing to shorter Fe-O bond-lengths, significant covalent bonding occurs between Fe-O, leading to a finite magnetic moment of 0.2 μ_B at oxygen sites. In the ground-state antiferromagnetic configuration, magnetic moments at octahedral Fe sublattice and tetrahedral Fe sublattice are oppositely aligned. As there are two tetrahedral Fe atoms for every octahedral atom, the moments are not cancelling each other resulting in a finite total magnetic moment and hence resulting in a ferrimagnetic configuration. The magnetic moments at Fe1^o and Fe2^t are 4.29 μ_B and 4.23 μ_B , respectively, and a total moment of 4.79 μ_B /f.u in the ferrimagnetic state. The oxygen atoms also have a moment of 0.16 μ_B , due to covalent contribution. The magnitude of magnetic moments increases with increase in U values. It may be noted that the ferrimagnetic configuration is lower in energy (by ~ 3 eV) than ferromagnetic configuration implying that ferrimagnetic state is energetically more favorable, for different U values. As we obtained insulating ground state for a similar oxide⁷⁵ for $U=6$ eV and $J=1$ eV, we used the same values to study electronic structure of Lu₃Fe₅O₁₂ also.

The calculated total density of states (DOS) is shown in Fig. 6 to obtain more insight on electronic structure of Lu₃Fe₅O₁₂ in ferro and ferrimagnetic configurations. Interestingly, a finite energy gap of 1.39 eV can be seen between valence band (below Fermi level; E_F) and conduction band (above E_F) in ferromagnetic configuration. It may be noted that

ferromagnetic insulators are seldom observed and receive wide attention for potential applications in spintronic devices. Hence, if $\text{Lu}_3\text{Fe}_5\text{O}_{12}$ could be stabilized in ferromagnetic configuration, it would be useful for technological applications. The system remains in insulating state in ferrimagnetic configuration as well, with an increased band gap of 1.66 eV. The atom-projected DOS in ferrimagnetic state is shown in Fig. 7. The valence band in top-most panel showing Lu states is almost empty, indicating that Lu has donated its valence electrons and hence forms ionic bond with its neighbors. The Fe DOS are prominently seen between -8 to 0 eV. As O *p*-states are visible between -4 to 0 eV, strong covalent bond between Fe and O can occur in this energy range. It may be noted that electronic states either participate in bonding or magnetic interaction. The presence of Fe DOS at ~ -6 eV is significant and strongly localized, indicating their significant contribution to magnetic-moment of Fe atoms. As the calculated magnetic moments and DOS features are almost similar for $\text{Fe}^{1\circ}$ and $\text{Fe}^{2\text{t}}$, it can be inferred that both Fe atoms could be in 3+ valence states. However, it may be noted that perfectly stoichiometric composition is considered in our theoretical calculation because including oxygen vacancies will require formation of larger supercells and hence computations become intensive. On the other hand experimental samples have significant oxygen vacancies. The presence of Fe^{2+} ions can be confirmed theoretically only when oxygen vacancies are included in the calculation.

4.7. Dielectric analysis

The existence of Fe^{3+} and Fe^{2+} ions renders the material dipoles and their arrangement in the direction of applied electric field produces electric polarization. The change in dielectric permittivity (ϵ') i.e., deciding factor of polarization as a function of temperature (353 K - 723 K) for different frequencies (1 kHz – 1 MHz) is seen in Fig. 8. The dielectric permittivity linearly increases with increase in temperature upto 550 K, above which starts to increase anomalously. This anomalous behavior is due to the fact that the temperature effect on Fe^{2+}

and Fe^{3+} ions produces a large shift in the electric dipole moment corresponding to polarization. The increase in ϵ' shows a maximum with a peak around 625 K and then decreases with further increase in temperature. This type of behaviour is usually seen in ferroelectric materials that undergo a phase transition from ferroelectric to non-ferroelectric (paraelectric) phase. The aforesaid phase transition can be confirmed using the $d(1/\epsilon')/dT$ versus temperature plot (inset of Fig. 8). From the plot, it is observed that there is no variation corresponding to the peak at 625 K. This clearly shows that, the peak appeared in the dielectric plot (Fig. 8) is not due to ferroelectric phase transition. The P - E loop recorded at room temperature with an applied field of 10 Vcm^{-1} also confirms the non-ferroelectric nature of the compound (Fig. 9). Therefore, the observed behaviour is completely consistent with linear capacitor behaviour, which is the characteristic of a lossy capacitor.^{76,77} Hence, the peak in the dielectric permittivity plot may be due to space charge polarization associated with oxygen vacancies.

Coming back to the dielectric plot, the dielectric anomaly starts in the vicinity of 550 K above which the magnetic ordering disappears. This is an effect of vanishing magnetic order around this temperature, which was predicted by Landau-Devonshire theory of phase transition.⁷⁸ This is ascertained from the inset of Fig. 8, where a sharp fall is clearly observed around 550 K. The possible appearance of dielectric anomalies around the magnetic ordering temperature result from the strong competition and interplay among the charge, orbital and spin degrees of freedom.^{7,79,80} Therefore, the dielectric anomaly starts at the vicinity of magnetic ordering temperature due to the coupling effect of dielectric and magnetic order parameters and this also explains the material's intrinsic MD property.

4.8. Magnetic and dielectric order coupling

To further demonstrate the coupling between magnetic and dielectric order parameters, the variation in ϵ' as a function of the magnetic field i.e., $(\epsilon'(H) - \epsilon'(0)) / \epsilon'(0)$ is used,⁸¹ where $\epsilon'(H)$ and $\epsilon'(0)$ are dielectric permittivity with the applied field H and without field, respectively. The changes in ϵ' in the presence of magnetic field (up to 0.7 T) at various frequencies (1 kHz - 1 MHz) at room temperature is shown in Fig. 10. The temperature dependent ϵ' shows an anomaly around its magnetic transition point, which was often taken as an evidence for MD coupling⁸²⁻⁸⁴ and is clearly shown in the inset of Fig. 10. As aforementioned, Fe^{2+} and Fe^{3+} ions could produce local dipoles. When a magnetic field is applied, the spins of Fe^{2+} and Fe^{3+} ions are altered causing redistribution of charges and dipoles leading to change in polarization, resulting in the observed MD effect. Thus, the coupling between magnetic and dielectric order is evident. The change in ϵ' observed with a change in the applied magnetic field indicates strong coupling. The magnitude of MD coupling reaches a maximum of 6 % at 10^3 Hz for 0.2 T, which is among the higher values reported for single-phase materials at room temperature and low field.

5. Conclusions

$\text{Lu}_3\text{Fe}_5\text{O}_{12.8}$ ceramics were prepared using the conventional solid state reaction method. Rietveld refinement of X-ray diffraction pattern and Mössbauer spectrum suggest the possibility of Fe ion in two different oxygen environments in octahedra. The magnetic moment calculation combined with vibrating sample magnetometer and Mössbauer results indicate the presence of oxygen vacancies and also the existence of Fe^{2+} and Fe^{3+} in the octahedral position. Moreover, the X-ray photoelectron spectrum of Fe 2p peak clearly matches with Fe^{2+} and Fe^{3+} states. The combined results of XPS and VSM clearly support the presence of oxygen vacancies and the existence of Fe ions in mixed valence state. The crystal

structure and its parameters obtained from complete structural optimization using density functional theory-based calculations are consistent with the experimentally observed structural parameters. Furthermore, the calculations correctly reproduce the ferrimagnetic ground state on comparing total energies of paramagnetic, ferromagnetic, and antiferromagnetic configurations. Electronic structure analysis provides more insight into the bonding characteristics and indicates mixed ionic-covalent bonding between various constituents. The calculated magnetic moments at octahedral and tetrahedral sites for ideal $\text{Lu}_3\text{Fe}_5\text{O}_{12}$ are not significantly different because the magnitude of exchange splitting in these sites is almost same. A non-negligible magnetic moment of $0.16 \mu_B$ at oxygen sites indicates significant covalent interaction between Fe and O atoms. However, theoretical calculations were carried out for perfectly stoichiometric composition and the oxygen vacancies present in the synthesized sample were not included in the calculations. Dielectric anomaly at the vicinity of magnetic ordering temperature indicates coupling between the magnetic and dielectric order parameters. Using an indigenously developed experimental setup, a low field magneto-dielectric response of about 6 % is observed at room temperature. The considerable magneto-dielectric response of $\text{Lu}_3\text{Fe}_5\text{O}_{12-\delta}$, even for a small applied field, makes it a candidate material for application in magneto-dielectric devices.

Acknowledgments

The author Dr P. Manimuthu (PM) thanks the University of Madras for the award of University Research Fellowship (UGC-URF-2009) and Council of Scientific and Industrial Research for the award of Senior Research Fellow (CSIR-SRF-2012). Dr R. Vidya (RV) thanks Research Council of Norway for computational time at Norwegian supercomputer consortium (NOTUR). PM also thanks Dr R. Murugaraj for his kind help in various aspects.

References

- 1 Kimura T, Goto T, Shintani H, Ishizaka K, Arima T and Tokura Y 2003 *Nature* **426** 55.
- 2 Hur N, Park S, Sharma P A, Ahn J S and Cheong S. W 2004 *Nature* **429** 392.
- 3 Weber S, Lunkenheimer P, Fichtl R, Hemberger J, Tsurkan V and Loidl A 2006 *Phys. Rev. Lett.* **96** 157202.
- 4 Spaldin N A and Fiebig M 2005 *Science* **309** 391.
- 5 Eerenstein W, Mathur N D and Scott J F 2006 *Nature* **442** 759.
- 6 Wang J, Neaton J B, Zheng H, Nagarajan V, Ogale S B, Liu B, Viehland D, Vaithyanathan V, Schlom D G, Waghmare U V, Spaldin N A, Rabe K M, Wuttig M and Ramesh R 2003 *Science* **299** 1719.
- 7 Mamin R F, Egami T, Marton Z and Migachev S A 2007 *Phys. Rev. B* **75** 115129.
- 8 Lorenz B, Litvinchuk A P, Gospondinov M M and Chu C W 2004 *Phys. Rev. Lett.* **92** 087204.
- 9 Zheng H, Wang J, Lofland S E, Ma Z, Mohaddes-Ardabili L, Zhao T, Salamanca-Riba L, Shinde S R, Ogale S B, Bai F, Viehland D, Jia Y, Schlom D G, Wuttig M, Roytburd A and Ramesh R 2004 *Science* **303** 661.
- 10 Dong S, Li J F and Viehland D 2003 *Appl. Phys. Lett.* **83** 2265.
- 11 Landau L D, Lifshitz E M and Pitaevskii L P 1984 *Electrodynamics of Continuous Media* (Pergamon, New York).
- 12 Jiang Q and Gong S. J 2005 *Eur. Phys. J. B* **43** 333.
- 13 Lorenz B, Wang Y Q, Sun Y Y and Chu C W 2004 *Phys. Rev. B* **70** 212412.
- 14 Rairigh R P, Singh-Bhalla G, Tongay S, Dhakal T, Biswas A and Hebard A. F 2007 *Nat. Phys.* **3** 551.
- 15 Katsufuji T and Takagi H 2001 *Phys. Rev. B* **64** 054415.

- 16 Kimura T, Kawamoto S, Yamada I, Azuma M, Takano M and Tokura Y 2003 *Phys. Rev. B* **67** 180401.
- 17 Hur N, Park S, Guha S, Borissov A, Kiryukhin V and Cheong S-W 2005 *Appl. Phys. Lett.* **87** 042901.
- 18 Suzuki T and Katsufuji T 2008 *Phys. Rev. B* **77** 220402 (R).
- 19 Yamasaki Y, Kohara Y and Tokura Y 2009 *Phys. Rev. B* **80** 140412.
- 20 Wu X B, Wang X F, Liu Y F, Cai W, Huang F Z, Lu X M and Zhu J S 2009 *Appl. Phys. Lett.* **95** 182903.
- 21 Scott J F 1979 *Rep. Prog. Phys.* **12** 1055.
- 22 Nugroho A A, Bellido N, Adem U, N'enert G, Simon C, Tija M O, Mostovoy M and Palstra T. T. M 2007 *Phys. Rev. B* **75** 174435.
- 23 Lal H B, Srivastava R and Srivastava K G 1967 *Phys. Rev.* **154** 505.
- 24 Sekine T and Katsura T 1976 *Solid State Chem.* **17** 49.
- 25 Manimuthu P, Jamal Ghousia Marriam M N, Murugaraj R and Venkateswaran C 2014 *Phys. Lett. A* **378** 1402.
- 26 Kohara Y, Yamasaki Y, Onose Y and Tokura Y 2010 *Phys. Rev. B* **82** 104419.
- 27 Su J, Lu X M, Zhang C, Zhang J T, Peng S, Wu X B, Min K L, Huang F Z and Zhu J S 2011 *J. Mater. Sci.* **46** 3488.
- 28 Lin Y Q and Chen X M 2010 *Appl. Phys. Lett.* **96** 142902.
- 29 Manimuthu P and Venkateswaran C 2012 *J. Phys. D: Appl. Phys.* **45** 015303.
- 30 Vijaya Kumar M S, Kuribayashi K and Kitazono K 2008 *J. Mater. Res.* **23** 2996.
- 31 Rietveld H M 1967 *Acta Crystallogr.* **22** 151.
- 32 Larson A C and Von Dreele R B 1994 *General Structure Analysis System (GSAS)* (Los Alamos Laboratory Report LAUR, 86-748).

- 33 Manimuthu P, Praveen Shanker H, Saravana Kumar K and Venkateswaran C 2014 *Physica B: Cond. Matt.* **448** 354.
- 34 Kresse G and Hafner J 1993 *Phys. Rev. B* **47** R6726; Kresse G and Furthmuller J 1996 *Comput. Mater. Sci.* **6** 15.
- 35 Blöchl P E 1994 *Phys. Rev. B* **50** 17953.
- 36 Kresse G and Joubert J 1999 *Phys. Rev. B* **59** 1758.
- 37 Kohn W and Sham L J 1965 *Phys. Rev.* **136** B864.
- 38 Payne M C, Teter M, Allen D C, Arias T A and Joannopoulos J D 1992 *Rev. Mod. Phys.* **64** 1045.
- 39 Pulay P 1980 *Chem. Phys. Lett.* **73** 393.
- 40 Perdew J P 1991 in *Electronic Structure of Solids*, edited by Ziesche P and Eschrig H (Akademie Verlag, Berlin); Perdew J P, Burke K and Wang Y 1996 *Phys. Rev. B* **54** 16533, Perdew J P, Burke K and Ernzerhof M 1996 *Phys. Rev. Lett.* **77** 3865.
- 41 Dudarev S L, Botton G A, Savrasov S Y, Humphreys C J and Sutton A P 1998 *Phys. Rev. B* **57** 1505.
- 42 Elsässer C, Fähnle M, Chen C T and Ho K M 1994 *Phys. Rev. B* **49** 13975.
- 43 Shannon R D and Prewitt C T 1969 *Acta Cryst. B* **25** 925; 1970 *B* **26** 1046.
- 44 Pascard H 1984 *Phys. Rev. B* **30** 2299.
- 45 Bourgeois J, Hervieu M, Poienar M, Abakumov A M, Elkaim E, Sougrati M T, Porcher F, Damay F, Rouquette J, Van Tendeloo G, Maignan A, Haines J and Martin C 2012 *Phys. Rev. B* **85** 064102.
- 46 Makarova O L, Bourgeois J, Poienar M, Mirebeau I, Kichanov S E, Andre G, Elkaim E, Hanfland M, Hervieu M, Maignan A, Haines J, Rouquette J, Martin C and Damay F 2013 *Appl. Phys. Lett.* **103** 082907.
- 47 Shannon R D 1976 *Acta Cryst. A* **32** 751.

- 48 Geller S, Williams H J, Sherwood R C and Espinosa G P 1962 *J. App. Phys.* **33** 1195.
- 49 Hoskins B F and Martin R L 1995 *Aust. J. Chem.* **48** 709.
- 50 Skorodumova N V, Simak S I, Lundqvist B I, Abrikosov I A and Johansson B 2002 *Phys. Rev. Lett.* **89** 166601.
- 51 Esch F, Fabris S, Zhou L, Montini T, Africh C, Fornasiero P, Comelli G and Rosei R 2005 *Science* **309** 752.
- 52 Brown I D and Altermatt D 1985 *Acta Crys.* **841** 244.
- 53 Ichida H, Nagai K, Sasaki Y and Pope M T 1989 *J. Am. Chem. Soc.* **111** 586.
- 54 Finke R G, Rapko B and Weakley T J R 1989 *Inorg. Chem.* **28** 1573.
- 55 Bucholz N, LeimkUhler M, Kiriazis L and Mattes R 1988 *Inorg. Chem.* **27** 2035.
- 56 Palenik G J and Hu S Z 2009 *Inorg. Chim. Acta* **362** 4740.
- 57 de Groot J, Mueller T, Rosenberg R A, Keavney D J, Islam Z, Kim J -W and Angst M 2012 *Phys. Rev. Lett.* **108** 187601.
- 58 Zhou Z, Guo L, Yang H, Liu Q and Ye F 2014 *J. Alloy. Comp.* **583** 21.
- 59 Thorp H H 1992 *Inorg. Chem.* **31** 1585.
- 60 Brown I D 2009 *Chem. Revs.* **109** 6858.
- 61 Brown I D 2002 *The Chemical Bond in Inorganic Chemistry* (Oxford University Press, Oxford, UK).
- 62 Greenwood N N and Gibb T C 1971 *Mössbauer Spectroscopy* (Chapman and Hall, London).
- 63 Lataifeh M S, Mahmood S and Thomas M F 2002 *Physica B* **321** 143.
- 64 Paesano Jr A, Zanatta S C, De Medeiros S N, Cotica L F and Da Cunha J B M 2005 *Hyperfine Interact.* **161** 211.
- 65 Zhe L, Shinno I, Danian Y, Pingqiu F and Yueming Z 2001 *Science in China (Series D)* **44** 34.

- 66 Bancroft G M 1973 *Mössbauer spectroscopy: An Introduction for Inorganic Chemists and Geochemists* (McGraw-Hill, London).
- 67 Ravindran P, Vidya R, Fjellvåg H and Kjekshus A 2008 *Phys. Rev. B* **77** 134448.
- 68 Grosvenor P, Kobe B A, Biesinger M C and McIntyre N S 2004 *Surf. Interface Anal.* **36** 1564.
- 69 Suchomski C, Reitz C, Sousa C T, Arango J P and Brezesinski T 2013 *Chem. Mater.* **25** 2527.
- 70 Yamashita T and Hayes P 2008 *Appl. Surf. Sci.* **254** 2441.
- 71 Moulder J F, Stickle W F, Sobol P E, Bomben K D, Chastain J and King R C 1995 Jr, *Handbook of X-ray photoelectron spectroscopy* (ULVAC-PHI, Inc, Japan).
- 72 Mills P and Sullivan J L 1983 *J. Phys. D: Appl. Phys.* **16** 723.
- 73 Hawn D D and DeKoven B M 1987 *Surf. Interface Anal.* **10** 63.
- 74 Basset J B, Denny R C, Jeffery G H and Mendham J 1978 *Vogels Text Book of Quantitative Inorganic Analysis* (London, UK: Longman Scientific and Technical).
- 75 Vidya R, Ravindran P, Knizek K, Kjekshus A and Fjellvåg H 2008 *Inorg. Chem.* **47** (15) 6608.
- 76 Scott J F 2008 *J. Phys.: Condens. Matter* **20** 021001.
- 77 Scott J F 1989 *JETP Lett.* **49** 233.
- 78 Benguigui L 1972 *Solid State Comm.* **11** 825.
- 79 Zhong B G, Mu R W and Fang J H 2005 *Solid State Comm.* **135** 759.
- 80 Su J, Lu X, Zhang C, Zhang J, Sun H, Ju C, Wang Z, Min K, Huang F and Zhu J 2012 *Physica B* **407** 485.
- 81 Cui Y F, Zhao Y G, Luo L B, Yang J J, Chang H, Zhu M H, Xie D and Ren T L 2010 *Appl. Phys. Lett.* **97** 222904.

82 Singh A K, Kaushik S D, Kumar B, Mishra P K, Venimadhav A, Siruguri V and Patnaik S
2008 *Appl. Phys. Lett.* **92** 132910.

83 Bhattacharjee S, Panday V, Kotnala R K and Panday D 2009 *Appl. Phys. Lett.* **94** 012906.

84 Chikara S, Karneta O, Crummett W P, DeLong L E, Schlottmann P and Cao G 2010
J. Appl. Phys. **107** 09D910.

List of Figure captions

Fig. 1. (a) Magnetic structure of $\text{Lu}_3\text{Fe}_5\text{O}_{12}$. View of (b) octahedra and (c) tetrahedra.

Fig. 2. Rietveld refinement of $\text{Lu}_3\text{Fe}_5\text{O}_{12-\delta}$ X-ray diffraction pattern.

Fig. 3. Mössbauer spectrum indicating three sextets of Fe ions in the tetrahedral and octahedral sites. Open circle represents the experimental data and continuous line indicates overall fit. The symbols (\cdot), ($*$), and ($+$) indicates $\text{Fe}_1 1^\circ$, $\text{Fe}_2 1^\circ$, and Fe_2^t , respectively.

Fig. 4. (a) Magnetization vs magnetic field showing clear ferrimagnetic behavior at 30 K and 300 K, inset shows the enlarged view. (b). Temperature dependent magnetization curve of $\text{Lu}_3\text{Fe}_5\text{O}_{12-\delta}$, inset shows the first derivative plot indicating paramagnetic to ferrimagnetic transition at 550 K.

Fig. 5. High resolution X-ray photoelectron spectrum of the Fe 2p peak.

Fig. 6. Total density of states calculated with LDA+ U method for ferromagnetic and ferrimagnetic configurations.

Fig. 7. Atom-specific density of states in ferrimagnetic configuration. The vertical dashed line at '0' indicates Fermi level.

Fig. 8. Temperature dependent ϵ' for different frequency values shows the dielectric anomaly starts around 550 K. Inset shows the first derivative plot of $1/\epsilon'$.

Fig. 9. Room temperature P - E loop showing linear capacitor behaviour.

Fig. 10. Magneto-dielectric measurement showing coupling between magnetic and dielectric orders at room temperature. Inset shows clearly the anomaly of dielectric permittivity present at the magnetic ordering temperature.

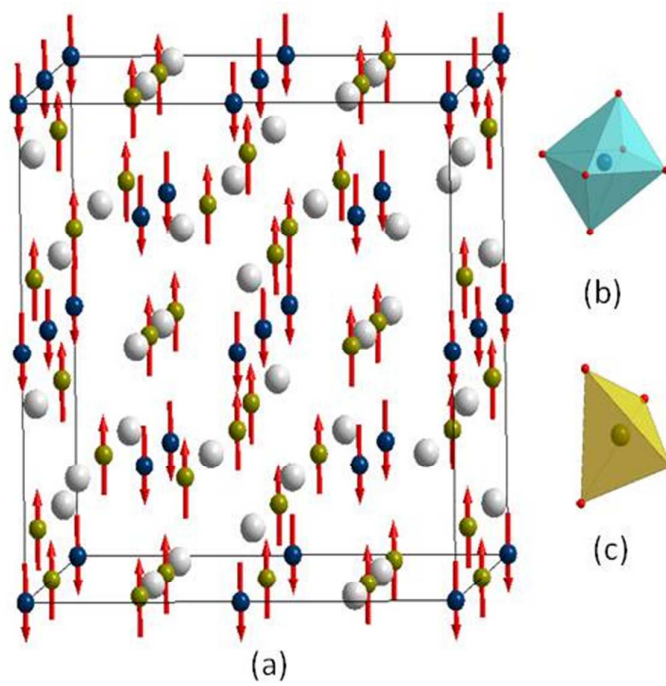


Fig. 1

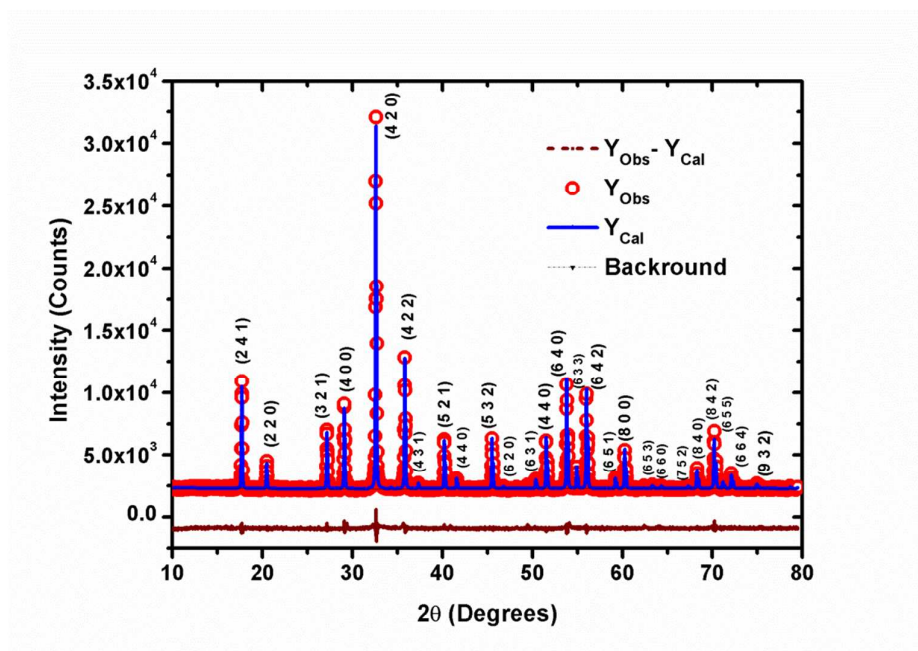


Fig. 2

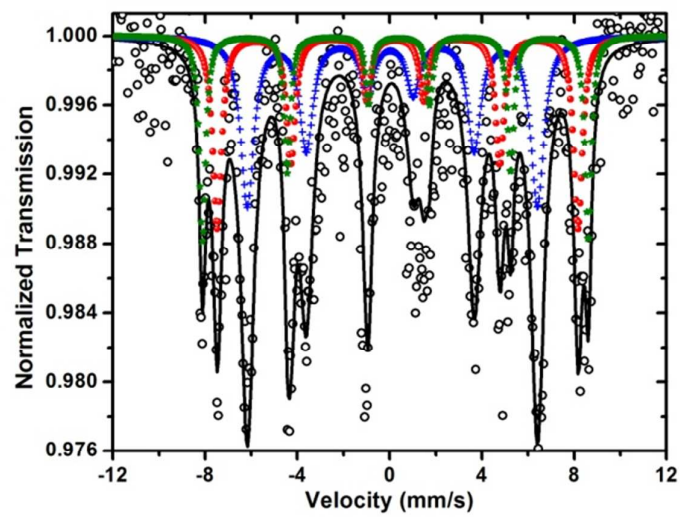


Fig. 3

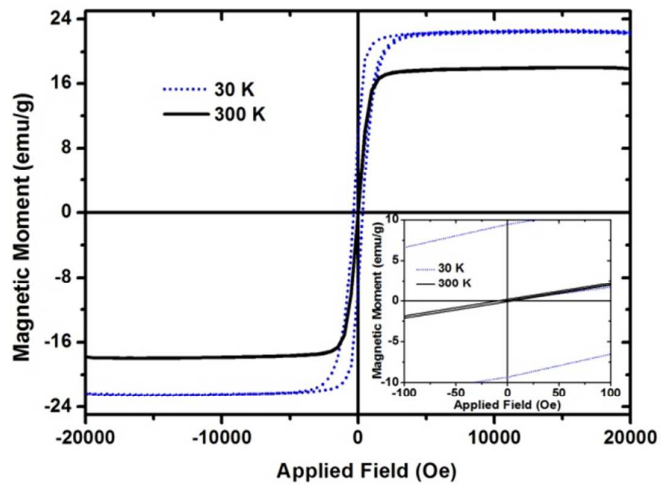


Fig. 4(a)

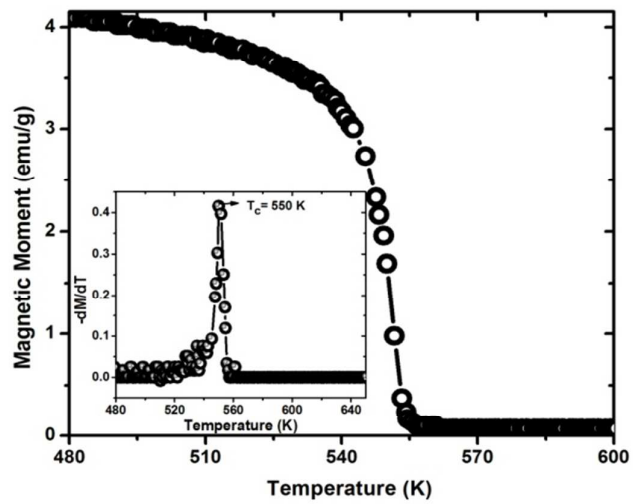


Fig. 4(b)

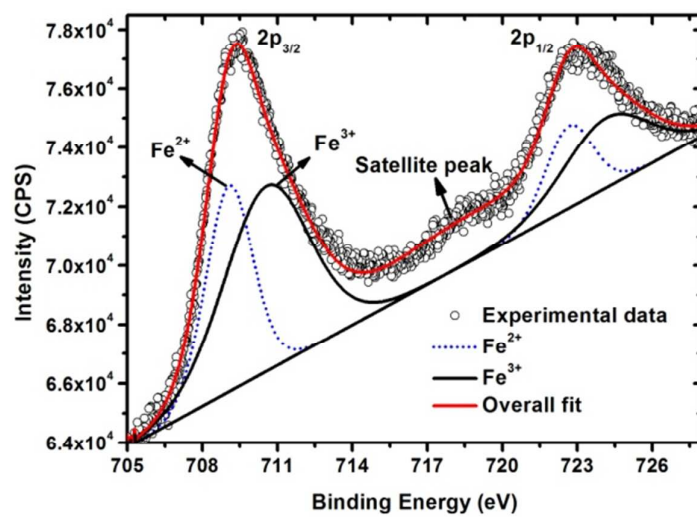


Fig. 5

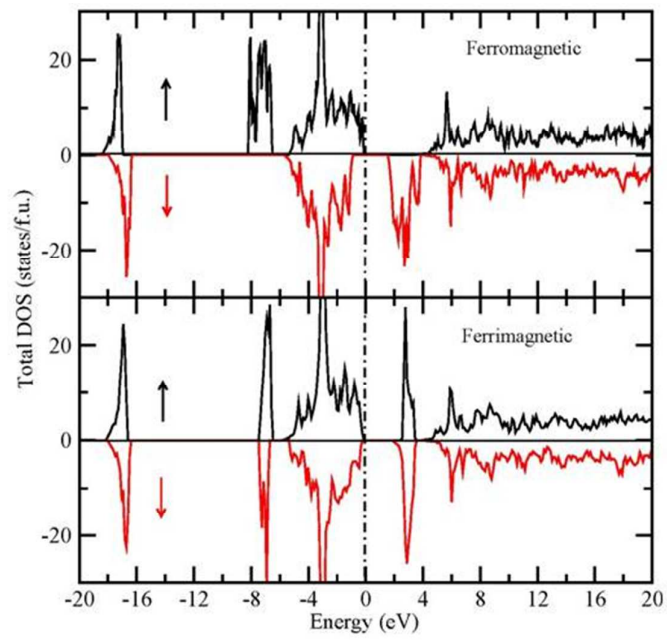


Fig. 6

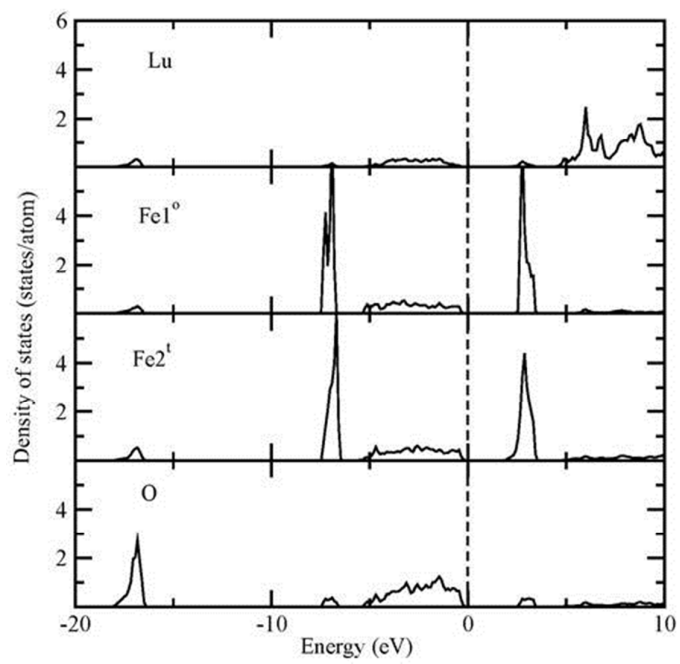


Fig. 7

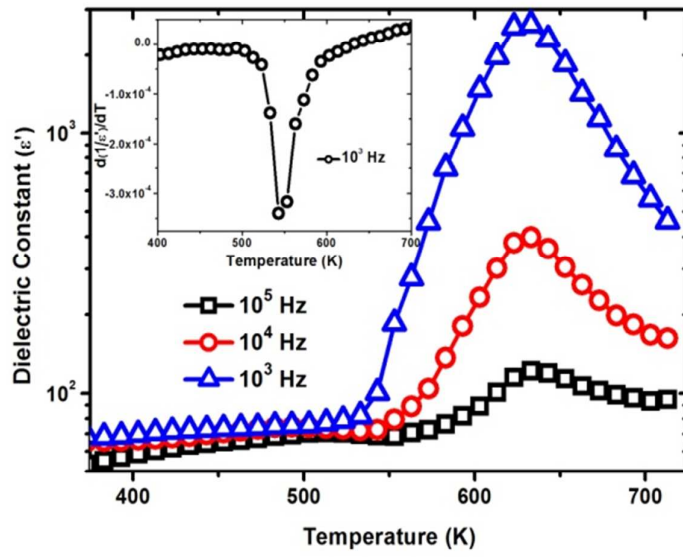


Fig. 8

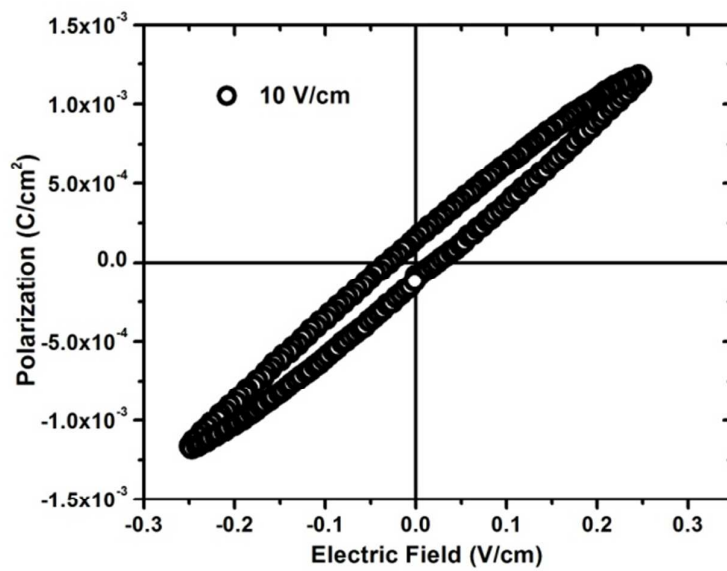


Fig. 9

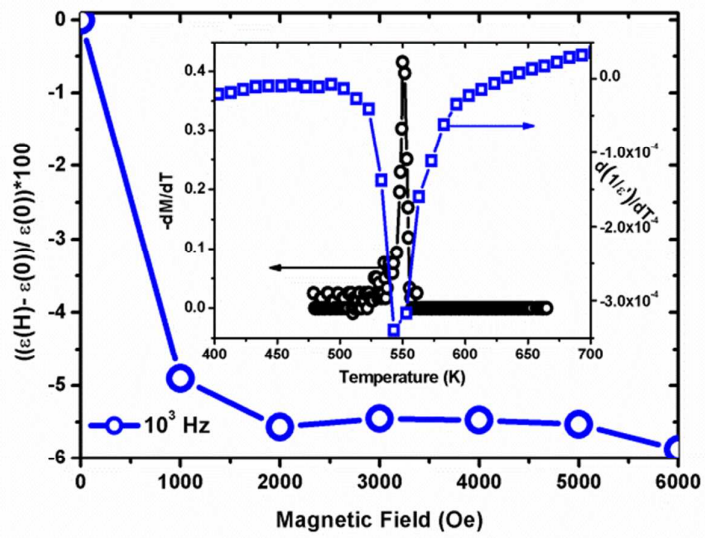


Fig. 10

Table I. Optimized structural parameters and atom positions derived from Rietveld refinement of XRD pattern.

Atom	Oxidation State	Position coordinates			Wyckoff position	B-factor	Occupancy	Cell parameter	
		x	y	z				'a' in Å	Volume in Å ³
Lu1	Lu ³⁺	0.1250	0.0000	0.2500	24c	0.02669	1	12.279(2)	1851.1(1)
Fe1 ^o	Fe ³⁺ /Fe ²⁺	0.0000	0.0000	0.0000	16a	0.03366	1		
Fe2 ^t	Fe ³⁺	0.3750	0.0000	0.2500	24d	0.02417	1		
O1	O ²⁻	-0.02743	0.0575	0.15218	96h	0.03815	1		

Table II. Optimized structural parameters and atom positions derived from DFT calculation.

Atom	Oxidation State	Position coordinates			Wyckoff position	Occupancy	Cell parameter	
		x	y	z			'a' in Å	Volume in Å ³
Lu1	Lu ³⁺	0.1250	0.0000	0.2500	24c	1	12.3901	1902
Fe1 ^o	Fe ³⁺	0.0000	0.0000	0.0000	16a	1		
Fe2 ^t	Fe ³⁺	0.3750	0.0000	0.2500	24d	1		
O1	O ²⁻	-0.02588	0.0548	0.15125	96h	1		

Table III. The magnetic moments calculated at ferromagnetic and ferrimagnetic configurations for various U values.

U value	Ferromagnetic configuration			Ferrimagnetic configuration		
	Fe1 ^o (μ_B)	Fe2 ^t (μ_B)	Total ($\mu_B/f.u.$)	Fe1 ^o (μ_B)	Fe2 ^t (μ_B)	Total ($\mu_B/f.u.$)
3 eV	4.20	4.05	24.05	4.0	3.91	4.64
4 eV	4.29	4.13	24.19	4.11	4.01	4.69
5 eV	4.36	4.21	24.33	4.20	4.11	4.74
6 eV	4.43	4.29	24.49	4.29	4.23	4.79